



Generalized Stress–Strain Curves for IBII Tests on Isotropic and Orthotropic Materials

F. Pierron¹ · L. Fletcher¹

Received: 4 February 2019 / Accepted: 16 April 2019
© The Author(s) 2019

Abstract

This article presents a particular use of the Virtual Fields Method to exploit the results of Image-Based Inertial Impact (IBII) tests. This test consists on an edge-on impact of a free-standing thin flat rectangular coupon. The specimen response is recorded using an ultra-high speed camera filming the deformation of a grid pattern printed at its surface. From these images, displacement fields are derived, from which strain and acceleration can be obtained. The Virtual Fields Method makes use of the acceleration fields to derive stress information. Until now, a very simple ‘stress-gauge’ approach was used that could only provide relevant stress-strain information if the test was predominantly uniaxial. The alternative was to use the full inverse approach with the Virtual Fields Method but this would not allow the same degree of data understanding as the ‘stress-gauge’ approach. This article proposes an extension to this ‘stress-gauge’ approach for fully multiaxial tests. The equations are first derived and then validated using simulated and experimental IBII test data on isotropic and orthotropic materials.

Keywords High strain rate · High speed imaging · Grid method · Virtual fields method · Composites

Introduction

Many engineering materials exhibit time-dependent properties. In the case of fast transient loadings like crash, blast or impact, the behaviour of a given structure can only be predicted if an accurate representation of the strain rate dependence of its constituent materials is available. While for certain classes of problems, high rate behaviour can be deduced from low rate tests [1], generally, this is not available and high strain rate tests have to be conducted. One of the main difficulties in high rate testing concerns the measurement of the applied load. For drop-weight and fast hydraulic machines, the propagation of transient waves in the load cell causes ringing which prevents accurate measurement of the load sustained by the specimen. In Hopkinson bar systems, the transient waves propagating in the specimen violate the

necessary quasi-static equilibrium required to perform the data reduction [2].

The advent of modern ultra-high speed imaging systems based on single sensors [3–6] in the late 2000s has democratized the recording of videos in the MHz range, making it possible to record images encoding the deformation associated with elastic mechanical waves arising from impact load. Using surface patterns, like a random speckle or a regular cross-hatch grid, at the surface of the test piece, it is then possible to extract space and time resolved displacements using image correlation [7] or phase-shifting [8] image processing techniques. One of the key features that this enables is the derivation of time resolved acceleration maps. Combined with the dynamic mechanical equilibrium equations of a continuous solid, for instance expressed by the Principle of Virtual Work, acceleration maps provide direct stress information thus avoiding the need for external load measurement. The load information becomes embedded into the images and both stress and strain can be simultaneously extracted from them [9].

The first publications to exploit this new paradigm appeared in the late 2000s [10, 11] and it has flourished in the later part of the 2010s [12–17]. A modern implementation of this idea uses purely inertial test configurations, inspired by the spalling tests in [13]. The principle

✉ F. Pierron
f.pierron@soton.ac.uk

L. Fletcher
L.C.Fletcher@soton.ac.uk

¹ Faculty of Engineering and Physical Sciences, University of Southampton, Highfield campus, University Road, Southampton SO17 1BJ, UK

was first published in 2014 [9] on an elastically isotropic material. It was then refined and extended to several classes of materials under the name ‘Image-Based Inertial Impact’ (IBII) test [18–21]. This test consists of an edge-on impact of a thin rectangular test specimen with all other edges free from any constraints. This sends a compression wave into the specimen which reflects off the free edge as a tensile wave. The pulse length can be designed either to load and unload the specimen in compression [9, 18] or to develop enough tension after wave reflection so that tensile fracture occurs [19–21].

In this new class of high strain rate tests, two main approaches have been used to identify the constitutive parameters. The first one is based on a full implementation of the Virtual Fields Method (VFM), with parametrized constitutive models [12, 18, 22]. The second one uses a reconstruction of the average longitudinal stress across a vertical section of the test specimen to build up stress-strain curves, employing rigid-body-like virtual fields in the VFM. This has been referred to in the past as the ‘stress-gauge’ approach. In the case of isotropic materials, this requires the *a priori* knowledge of Poisson’s ratio or the assumption of uniaxial stress [9]. Poisson’s ratio can be obtained using the full VFM analysis [19], but it would be convenient to enable both stiffness components to be identified with a stress-gauge approach, which is the object of the present paper. For orthotropic materials tested ‘on-axis’ (i.e. with orthotropy axes aligned with the specimen axes), this is also possible. However, when a unidirectional composite is tested in the 90° orientation, Poisson’s effect can be neglected because of the high stiffness at 0° [19, 21]. The advantage of this second approach is that it leads naturally to spatially resolved properties, and provides an easy way to plot 2D curves from which the departure from possible linearity / elasticity is easily appraised.

In classical uniaxial tests, it is possible to plot stress versus strain to directly obtain Young’s modulus from the slope of the response in the linear range. However, this is generally not possible for multi-axial stress states when the stress field is unknown *a priori*, and inverse identification has to be used. Thanks to the possibility of reconstructing stress from acceleration in transient dynamics, the present article proposes a generalization of this stress-strain curve concept to the case of 2D multi-axial stress states for both isotropic and orthotropic IBII tests. The equations are first derived for isotropy. They are then extended to orthotropic properties by introducing the concept of an ‘angled stress-gauge’ for the first time. This is validated on FE and experimental data for isotropic and orthotropic off-axis IBII tests. The experiments consider a tungsten carbide cermet (isotropy, [20]) and a 45° carbon/epoxy unidirectional composite. It should be noted that the quantities derived here can be applied to alternative inertial tests like the Image-Based Ultrasonic Shaking

(IBUS) test. This test relies on an ultrasonic vibration to excite a thin rectangular test piece on its first resonance frequency to introduce high rate deformation [23].

Generalized Stress–Strain Curves in Isotropic Elasticity

The objective of this section is to present the derivation of equivalent stress-strain quantities that allow for the construction of generalized stress-strain curves for the case of isotropic elasticity.

Theoretical Derivation

The principle of the technique is based on the Virtual Fields Method employing rigid-body virtual fields to derive stress metrics independently from the constitutive model. The principle of virtual work can be written as follows:

$$-\int_V \sigma : \epsilon^* dV + \int_{\partial V_f} T \cdot u^* dS = \int_V \rho a \cdot u^* dS \quad (1)$$

where σ is the Cauchy stress tensor, T is the traction vectorial field at the boundary ∂V_f of the considered volume V , ρ is the material density and a is the acceleration field. The \star quantities, u^* and ϵ^* , are the virtual fields which act as test functions. The equation is valid for any u^* continuous and piecewise differentiable, with $2\epsilon_{ij}^* = [u_{ij}^* + u_{ji}^*]$.

It was shown in [9] that by using the virtual field $u_x^* = 1$ and $u_y^* = 0$ for the test configuration represented in Fig. 1, the following equation could be obtained:

$$\overline{\sigma_{xx}}^y = \rho x_0 \overline{a_x}^S \quad (2)$$

where $\overline{\sigma_{xx}}^y$ is the average of the longitudinal stress σ_{xx} over a vertical cross-section at $x = x_0$ and $\overline{a_x}^S$ is the average of the longitudinal acceleration over the area between the free edge and the considered section. It should be noted that this equation is always valid regardless of the constitutive

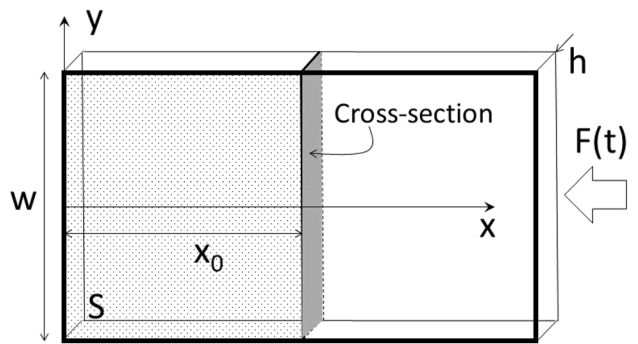


Fig. 1 Inertial impact test configuration from [9]

model of the material as it is purely based on equilibrium. The only - important - assumptions are that the mechanical fields are uniform through the thickness, the specimen is under a state of plane stress and that the material density is constant. The latter may be challenged for compactable materials but the density can be updated if necessary based

where Q_{11} and Q_{12} are the two plane stress stiffness components. Indexes (1, 2) are used here to distinguish the material from specimen axes, which is an unnecessary refinement for isotropy but will be necessary for the orthotropic section. This model can now be inserted into Eqs. 2, 3 and 4, providing the following equations:

$$\begin{cases} Q_{11}\overline{\epsilon_{xx}} + Q_{12}\overline{\epsilon_{yy}} = \rho x_0 \overline{a_x}^S & (1) \\ Q_{11}\overline{\epsilon_{xy}} - Q_{12}\overline{\epsilon_{xy}} = \rho x_0 \overline{a_y}^S & (2) \\ Q_{11}(\overline{\epsilon_{xx}y} - x_0 \overline{\epsilon_{xy}}) + Q_{12}(\overline{\epsilon_{yy}y} + x_0 \overline{\epsilon_{xy}}) = \rho x_0 (\overline{a_x y}^S - \overline{a_y x}^S) & (3) \end{cases} \quad (6)$$

on strain measurements [24]. Equation 2 was used in [9] to plot stress-strain curves for a quasi-isotropic carbon-epoxy composite, assuming either uni-axiality or a value for Poisson's ratio, see Fig. 14 in [9]. The advantage of this representation is that one can immediately see if the behaviour is linear, and witness possible damage or fracture, as in [13] or [25]. It was shown later [19] that two other rigid-body virtual fields could be used: $u_x^* = 0$ and $u_y^* = 1$, and $u_x^* = y$ and $u_y^* = -x$. They represent virtual rigid body movements in vertical translation and in-plane rotation. No others can be independently defined. The first one provides the following equation:

$$\overline{\sigma_{xy}^y} = \rho x_0 \overline{a_y}^S \quad (3)$$

where $\overline{\sigma_{xy}^y}$ is the average of the shear stress σ_{xy} over a vertical cross-sectional area at $x = x_0$ and $\overline{a_y}^S$ is the average of the transverse acceleration over the area between the free edge and the considered section. Finally, the rotational virtual field provides this equation [19]:

$$\overline{\sigma_{xx}y}^y - x_0 \overline{\sigma_{xy}^y} = \rho x_0 (\overline{a_x y}^S - \overline{a_y x}^S) \quad (4)$$

where $\overline{\sigma_{xx}y}^y$ is the average of σ_{xx} weighted by the vertical position of each point across the considered vertical slice (can also be seen as the average of the first moment of σ_{xx} with respect to the centre position of the slice); $\overline{a_x y}^S$ is the weighted average of a_x by transverse position and $\overline{a_y x}^S$ the weighted average of a_y by longitudinal position, both over surface S between the free edge and the section of coordinate x_0 .

It is now possible to exploit Eqs. 2, 3 and 4 further by combining them with a linear elastic constitutive model. Writing a plane stress isotropic linear-elastic model:

$$\begin{cases} \sigma_{xx} = Q_{11}\epsilon_{xx} + Q_{12}\epsilon_{yy} \\ \sigma_{xy} = (Q_{11} - Q_{12})\epsilon_{xy} \end{cases} \quad (5)$$

where a simple overline indicates averaging over a vertical line of data, superscript y has been abandoned to simplify the notation. Since there are two unknowns to be identified, any combination of two equations from the three above can be used. Each will provide an analytical expression in form of a generalized stress-strain relationship. The simplest form is obtained by combining equations ① and ② from Eq. 6. Solving for Q_{11} and Q_{12} in ②, feeding into ① and rearranging provides:

$$\begin{cases} Q_{11}(\overline{\epsilon_{xx}} + \overline{\epsilon_{yy}})\overline{\epsilon_{xy}} = \rho x_0 (\overline{a_x}^S \overline{\epsilon_{xy}} + \overline{a_y}^S \overline{\epsilon_{yy}}) \\ Q_{12}(\overline{\epsilon_{xx}} + \overline{\epsilon_{yy}})\overline{\epsilon_{xy}} = \rho x_0 (\overline{a_x}^S \overline{\epsilon_{xy}} - \overline{a_y}^S \overline{\epsilon_{xx}}) \end{cases} \quad (1+2) \quad (7)$$

For a perfectly linear elastic isotropic material, plotting $\rho x_0 (\overline{a_x}^S \overline{\epsilon_{xy}} + \overline{a_y}^S \overline{\epsilon_{yy}})$ as a function of $(\overline{\epsilon_{xx}} + \overline{\epsilon_{yy}})\overline{\epsilon_{xy}}$ should provide a straight line with a slope Q_{11} . Likewise, the second equation can also be plotted to obtain Q_{12} . The main advantage of this representation is that it provides a direct appraisal of the linearity of the response and can be used to detect the onset of damage or fracture. Also, because these curves can be plotted for all sections of the test specimen, this formulation can also provide a first evaluation of the homogeneity of the sample along the length. Finally, the resulting line plots are easy to read and have a form familiar to the experimental community used to uniaxial stress-strain curves. Obviously, the limitation is that if the material exhibits non-linear behaviour, these derivations will not hold any more and the full Virtual Fields Method will have to be employed, as in [18] for instance. However, the plots will show that the behaviour is not linear and as such, they remain a good diagnostics tool.

The other two combinations provide slightly more complex formulations that could be used to check the isotropy assumption for instance, as all combinations of virtual fields should provide the same stiffness values, barring the effect of noise. They are provided below.

$$\left\{ \begin{array}{l} Q_{11}(-\bar{\epsilon}_{xx}\bar{y} \bar{\epsilon}_{yy} + \bar{\epsilon}_{xx} \bar{\epsilon}_{yy}\bar{y} + x_0\bar{\epsilon}_{xy}[\bar{\epsilon}_{xx} + \bar{\epsilon}_{yy}]) = \\ \rho x_0 (\bar{\epsilon}_{yy}(\bar{a}_y\bar{x}^S - \bar{a}_x\bar{y}^S) + \bar{a}_x^S(x_0\bar{\epsilon}_{xy} + \bar{\epsilon}_{yy}\bar{y})) \\ Q_{12}(-\bar{\epsilon}_{xx}\bar{y} \bar{\epsilon}_{yy} + \bar{\epsilon}_{xx} \bar{\epsilon}_{yy}\bar{y} + x_0\bar{\epsilon}_{xy}[\bar{\epsilon}_{xx} + \bar{\epsilon}_{yy}]) = \\ \rho x_0 (\bar{\epsilon}_{xx}(\bar{a}_y\bar{x}^S - \bar{a}_y\bar{x}^S) + \bar{a}_x^S(x_0\bar{\epsilon}_{xy} - \bar{\epsilon}_{xx}\bar{y})) \end{array} \right. \quad (1+3)$$

$$\left\{ \begin{array}{l} Q_{11}(\bar{\epsilon}_{xx}\bar{y} + \bar{\epsilon}_{yy}\bar{y})\bar{\epsilon}_{xy} = \\ \rho x_0 (\bar{\epsilon}_{xy}(\bar{a}_x\bar{y}^S - \bar{a}_y\bar{x}^S + x_0\bar{a}_y) + \bar{a}_y \bar{\epsilon}_{yy}\bar{y}) \\ Q_{12}(\bar{\epsilon}_{xx}\bar{y} + \bar{\epsilon}_{yy}\bar{y})\bar{\epsilon}_{xy} = \\ \rho x_0 (\bar{\epsilon}_{xy}(\bar{a}_x\bar{y}^S - \bar{a}_y\bar{x}^S + x_0\bar{a}_y) - \bar{a}_y \bar{\epsilon}_{xx}\bar{y}) \end{array} \right. \quad (2+3)$$

Validation

Validation on Simulated Data

The data were generated using an explicit dynamics finite element model developed using ANSYS APDL LS-DYNA (v16.2). The model is formulated in 2D using the plane stress assumption and PLANE162 elements (4-noded, reduced integration). The geometrical model can be found in Fig. 2. The mesh consisted of 280 x 176 square elements. The time step was floating at 0.8 t_{crit} and the beta damping was set to 0.05. t_{crit} is the critical time step in the explicit analysis. The time step in the simulation must be smaller than this value to ensure stability. It corresponds to the shortest time taken for a dilatational wave to traverse an element in the simulation. This is calculated at each step for every element taking the minimum value of all elements. The minimum value is then multiplied by a safety factor (default of 0.8) to ensure

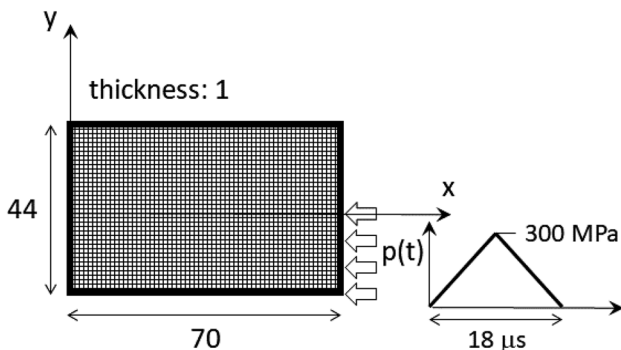


Fig. 2 Schematic of the isotropic finite element (FE) model used to validate the generalized stress-strain relationships (dimensions in mm)

stability of the simulation. Data was output at steps of 0.2 μ s to simulate acquisition of images at 5 Mfps with a Shimadzu HPV-X camera. A symmetrical triangular pressure pulse of peak value 300 MPa and width 18 μ s was applied over half the specimen width. The reason for this is that applying the pulse over the whole width resulted in highly symmetrical fields which made both sides of Eq. 4 close to zero. This illustrates very well the need for heterogeneity for such approaches to work. A linear elastic isotropic material was simulated with $E = 50$ GPa and $\nu = 0.3$, mimicking a carbon/epoxy quasi-isotropic material as in [9].

Both strains and accelerations were output at the nodal locations and used to calculate the spatial averages in Eqs. 7, 8 and 9 to produce the plots in Fig. 3. From the best linear fit of the curves in Fig. 3, the identified results are reported in Table 1. The results are very close to the reference ones, with the lowest error for the 1 + 2 combination, as expected since non-weighted averages are less sensitive to (numerical) noise.

Validation on Experimental Data

The equations above are now validated using experimental data from [20]. IBII tests were performed on Tungsten Carbide cermets with Cobalt and Nickel binders. The specimen considered here is 2-WC-F-13Co as reported in Table 5 in [20], which has 13% Cobalt binder. All experimental details are provided in this reference, only the main features are briefly recalled here. The specimens were $60 \times 30 \times 4$ mm³. They were impacted at a nominal speed of 50 m.s⁻¹. 15CDV6 high strength steel impactors and waveguides were used. Contrary to the simulation before, impact occurs over the full specimen width. The reason why this was possible here and not on the simulation is that experimentally, the boundary conditions are imperfect and some heterogeneity was present along vertical slices, which was enough to provide meaningful values for the two terms in Eq. 4. Grids were transferred onto the specimens using the technique detailed in [26]. A grid pitch of 0.7 mm was used. The grids were imaged at 5 Mfps with a Shimadzu HPV-X camera providing 400×250 pixel². The field of view was 56×35 mm². From the grid images, displacements were derived using the incremental version of the grid method as detailed in [8]. Acceleration and strain fields were then obtained by smoothing / differentiation, with details in [20].

The data were used to calculate the different terms in Eqs. 7, 8 and 9. The results are provided in Figs. 4, 5, 6. Combinations 1 + 2 provides the most linear response, followed by combination 1 + 3 and 2 + 3. They all lead to similar values for the stiffness, even though one would trust 1 + 2 more because of the lower effect of noise.

In fact, it is possible to identify these two stiffness components for all transverse sections. The results are illustrated in

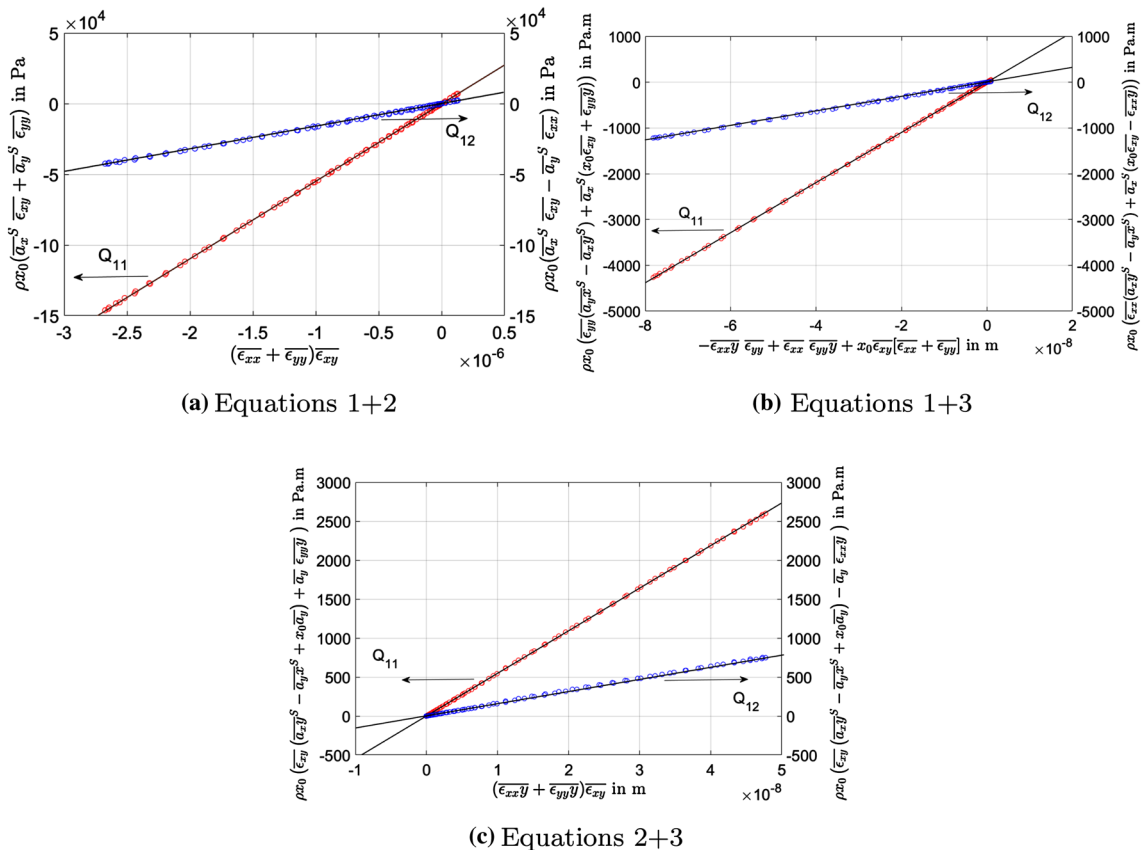


Fig. 3 Validation on isotropic FE generated data, section located at 30 mm from the free edge

Table 1 Identification results from FE simulated isotropic data

Stiffness in GPa	Q_{11}	Q_{12}
Reference	54.95	16.48
1 + 2	54.92	16.34
1 + 2 difference (%)	-0.04	-0.83
1 + 3	54.84	16.11
1 + 2 difference (%)	-0.18	-2.26
2 + 3	54.62	16.07
2 + 3 difference (%)	-0.57	-2.48

Fig. 7 for equations 1 + 2. The greyed out areas at both ends correspond to half the Gaussian smoothing kernel where the data are corrupted. In most of the central part of the specimen, the response is very stable with only small local variations of the identified stiffness, most probably caused by the measurement noise as this material is very stiff and does not deform much. However, between 38 and 50 mm, the modulus ramps up significantly. To investigate this, both terms of the first line of Eq. 7 were plotted for all time steps, as well as their difference. The results are shown in Fig. 8. The big red blob at the top of the difference map corresponds to the presence of a crack which clearly violates the

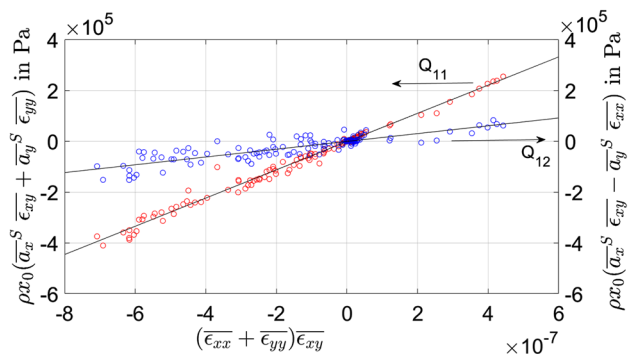


Fig. 4 Generalized stress-strain curve for experimental data on specimen 2-WC-F-13Co (Tungsten Carbide cermet) from [20], 16.7 mm from the free edge, equations 1 + 2. $Q_{11} = 555$ GPa, $Q_{12} = 153$ GPa, providing $E = 513$ GPa and $\nu = 0.28$

continuum assumption underlying the principle of virtual work on which this is based. It is also clear that down to about 40 mm from the free edge, the equation is well verified until the initiation of the crack. However, in the 15 mm closer to the impact edge, significant discrepancies exist, confirming the plot in Fig. 7. This is probably caused by uneven contact between the wave guide and the specimen,

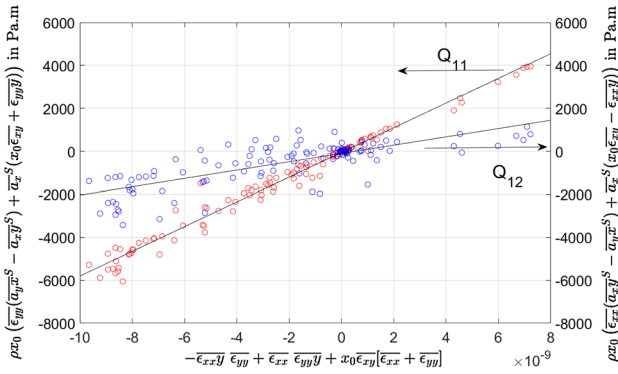


Fig. 5 Generalized stress-strain curve on experimental data for specimen 2-WC-F-13Co (Tungsten Carbide cermet) from [20], 16.7 mm from the free edge, equations 1 + 3. $Q_{11} = 575$ GPa, $Q_{12} = 193$ GPa, providing $E = 510$ GPa and $\nu = 0.34$

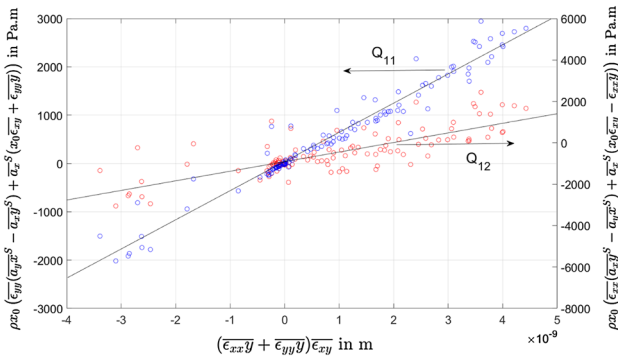


Fig. 6 Generalized stress-strain curve for experimental data on specimen 2-WC-F-13Co (Tungsten Carbide cermet) from [20], 16.7 mm from the free edge, equations 2 + 3. $Q_{11} = 602$ GPa, $Q_{12} = 198$ GPa, providing $E = 537$ GPa and $\nu = 0.33$

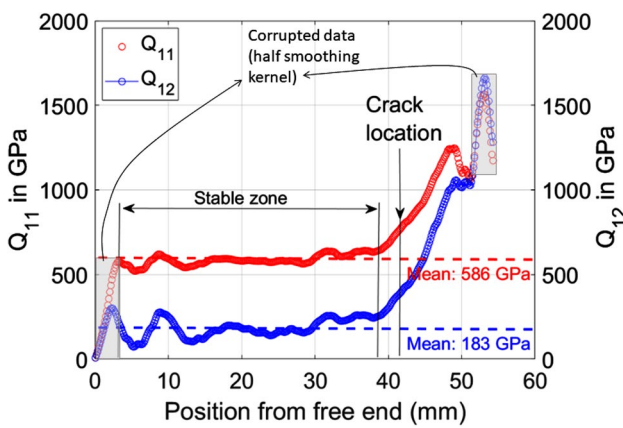


Fig. 7 Stiffness evolution in specimen 2-WC-F-13Co (Tungsten Carbide cermet) from [20], equations 1 + 2. The reported means correspond to the stable zone

which fades away a certain distance away from the impact. A similar effect was also reported in [27]. However, this would need to be confirmed by using back-to-back cameras to image both sides of the specimens in the future. Finally, the results from equations 1 + 3 and 2 + 3 show exactly the same trends, just with more oscillations on Q_{12} .

The identified stiffness values were averaged between 3 and 38 mm from the free edge based on the evidence in Fig. 7 and are reported in Table 2. Even though the noise is important for combinations 1 + 3 and 2 + 3, the stiffness data are consistent with those from 1 + 2. The results are consistent with that in [20] (Table 5). However, the analysis in [20] did not spot the inconsistencies of the data in the 12 mm closest to the impact edge. Table 2 reports the full VFM identification with optimized virtual fields excluding these 12 mm from the analysis. The Q_{11} values are now within 5% of each other. It is also worth noting that Getting *et al.* report a quasi-static value for E between 540 and 564 GPa for a similar material.

Generalized Stress–Strain Curves in Orthotropic Elasticity

Let us now consider a test specimen made of unidirectional composite material for which the fibres lie at a certain angle θ from the longitudinal axis x . Instead of considering a cross-section perpendicular to the test specimen, it is possible to use cross-sections parallel and perpendicular to the fibre direction, as represented in Fig. 9. In that case, rigid-body-like virtual fields can be defined in the coordinate system (x_1, x_2) associated with the fibre direction.

Section Parallel to the Fibres

This situation corresponds to the section represented on the left-hand side of Fig. 9. It will involve the Q_{22} , Q_{12} and Q_{66} stiffness components. The following virtual fields can be defined:

$$\begin{cases} u_1^{(1)*} = 0; u_2^{(1)*} = 1 \\ u_1^{(2)*} = 1; u_2^{(2)*} = 0 \\ u_1^{(3)*} = x_2; u_2^{(3)*} = -x_1 \end{cases} \quad (10)$$

Feeding this into the principle of virtual work, the following stress equations are obtained:

$$\begin{cases} \bar{\sigma}_{22}^{(x_2=0)} = \rho \frac{S_A}{b_A} \bar{a}_2^{S_A} \\ \bar{\sigma}_{12}^{(x_2=0)} = \rho \frac{S_A}{b_A} \bar{a}_1^{S_A} \\ -\bar{\sigma}_{22} x_1^{(x_2=0)} = \rho \frac{S_A}{b_A} \left(\bar{a}_1 x_2^{S_A} - \bar{a}_2 x_1^{S_A} \right) \end{cases} \quad (11)$$

Fig. 8 Two terms on each side of Eq. 7 and their difference, with $Q_{11} = 586$ GPa

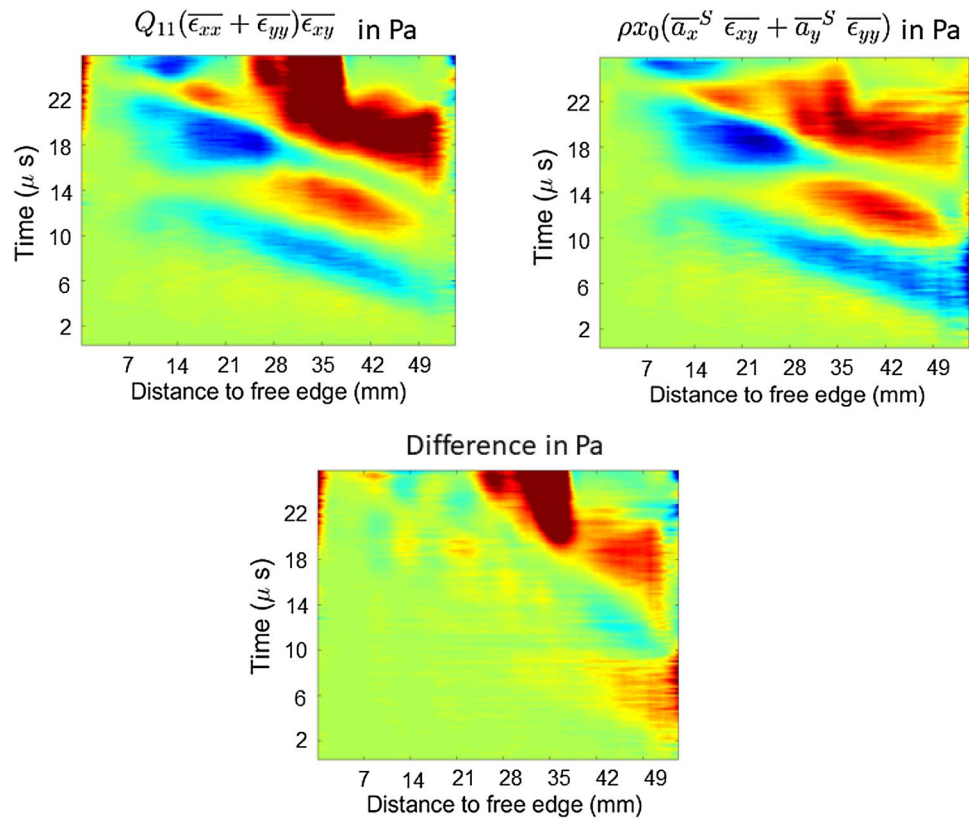


Table 2 Identification results the isotropic experimental data, specimen 2-WC-F-13Co (Tungsten Carbide cermet) from [20], averaged between 3 and 38 mm from the free edge

	Q_{11} (GPa)	Q_{12} (GPa)	E (GPa)	ν
Equations 1 + 2	586	183	529	0.31
Equations 1 + 3	584	173	532	0.30
Equations 2 + 3	582	178	527	0.31
[20] VFM (full FOV)	628	165	585	0.26
[20] VFM (restricted FOV)	565	135	533	0.24

where S_A is the surface area between the angled section and the free edge, and b_A is the length of the angled section (Fig. 9). To simplify the notation, line averages along ($x_2 = 0$) will be denoted with superscript l while surface area

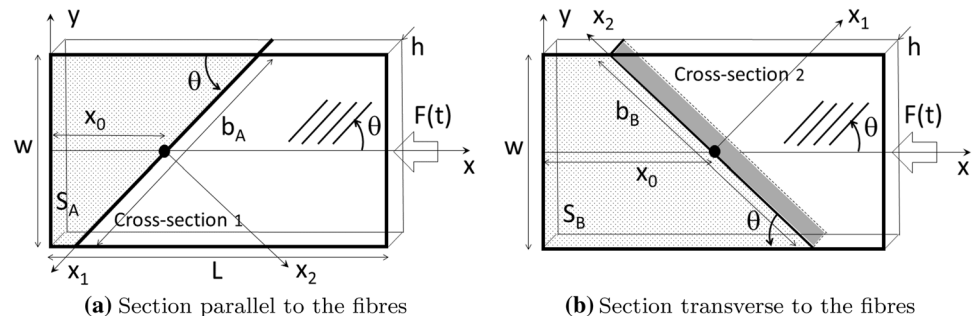
averages over S_A will be denoted with superscript S . The linear elastic orthotropic model can be written as:

$$\begin{cases} \sigma_{11} = Q_{11}\epsilon_{11} + Q_{12}\epsilon_{22} \\ \sigma_{22} = Q_{22}\epsilon_{22} + Q_{12}\epsilon_{11} \\ \sigma_{12} = 2Q_{66}\epsilon_{12} \end{cases} \quad (12)$$

Substituting into Eq. 11 leads to:

$$\begin{cases} Q_{22}\overline{\epsilon_{22}}^l + Q_{12}\overline{\epsilon_{11}}^l = \rho \frac{S_A}{b_A} \overline{a_2}^S \\ Q_{66}2\overline{\epsilon_{12}}^l = \rho \frac{S_A}{b_A} \overline{a_1}^S \\ -Q_{22}\overline{\epsilon_{22}x_1}^l - Q_{12}\overline{\epsilon_{11}x_1}^l = \rho \frac{S_A}{b_A} (\overline{a_1x_2}^S - \overline{a_2x_1}^S) \end{cases} \quad (13)$$

Fig. 9 Inertial impact test configuration for an off-axis orthotropic specimen



Solving for each individual stiffness component, the following relationship are obtained:

$$\begin{cases} Q_{22} (\bar{\epsilon}_{22}^l \bar{\epsilon}_{11} x_1^l - \bar{\epsilon}_{11}^l \bar{\epsilon}_{22} x_1^l) = \rho \frac{S_A}{b_A} ((\bar{a}_1 x_2^S - \bar{a}_2 x_1^S) \bar{\epsilon}_{11}^l + \bar{a}_2^S \bar{\epsilon}_{11} x_1^l) \text{ (O1)} \\ Q_{12} (\bar{\epsilon}_{11}^l \bar{\epsilon}_{22} x_1^l - \bar{\epsilon}_{22}^l \bar{\epsilon}_{11} x_1^l) = \rho \frac{S_A}{b_A} ((\bar{a}_1 x_2^S - \bar{a}_2 x_1^S) \bar{\epsilon}_{22}^l + \bar{a}_2^S \bar{\epsilon}_{22} x_1^l) \text{ (O2)} \\ Q_{66} 2 \bar{\epsilon}_{12}^l = \rho \frac{S_A}{b_A} \bar{a}_1^S \text{ (O3)} \end{cases} \quad (14)$$

Equations (O1) and (O2) are symmetrical with respect to ϵ_{11} and ϵ_{22} , as expected. In practice, for highly anisotropic carbon-epoxy composites, the strain in the fibre direction, ϵ_{11} , is likely to be very small. In this case, the term $Q_{12}\epsilon_{11}$ can be neglected with respect to $Q_{22}\epsilon_{22}$ in the second line of Eq. 12 and a simplified version of equation (O1), denoted (OS1) is obtained:

$$\left\{ Q_{22} \bar{\epsilon}_{22}^l = \rho \frac{S_A}{b_A} \bar{a}_2^S \right\} \text{ (OS1)} \quad (15)$$

For carbon/epoxy unidirectional composites, Equation (O2) will generally not be exploitable as both quantities to the right and left of the equation will be too small. This is akin to attempting to identify the minor Poisson's ratio on a 90° tensile test. However, for lower anisotropy materials like glass/

$$\begin{cases} \bar{\sigma}_{11}^{(x_1=0)} = \rho \frac{S_B}{b_B} \bar{a}_1^S \\ \bar{\sigma}_{12}^{(x_1=0)} = \rho \frac{S_B}{b_B} \bar{a}_2^S \\ \bar{\sigma}_{11} x_2^{(x_1=0)} = \rho \frac{S_B}{b_B} (\bar{a}_1 x_2^S - \bar{a}_2 x_1^S) \end{cases} \quad (17)$$

where S_A is the surface area between the angled section and the free edge, and b_A is the length of the angled section (Fig. 9). To simplify the notation, line averages along ($x_1 = 0$) will be denoted with superscript l while surface area averages over S_B will be denoted with superscript S . Using the constitutive equations in Eq. 12 and solving for individual stiffness components, the following relationships are obtained:

$$\begin{cases} Q_{11} (\bar{\epsilon}_{22}^l \bar{\epsilon}_{11} x_2^l - \bar{\epsilon}_{11}^l \bar{\epsilon}_{22} x_2^l) = \rho \frac{S_B}{b_B} ((\bar{a}_1 x_2^S - \bar{a}_2 x_1^S) \bar{\epsilon}_{22}^l - \bar{a}_1^S \bar{\epsilon}_{22} x_2^l) \text{ (O4)} \\ Q_{12} (\bar{\epsilon}_{11}^l \bar{\epsilon}_{22} x_2^l - \bar{\epsilon}_{22}^l \bar{\epsilon}_{11} x_2^l) = \rho \frac{S_B}{b_B} ((\bar{a}_1 x_2^S - \bar{a}_2 x_1^S) \bar{\epsilon}_{11}^l - \bar{a}_1^S \bar{\epsilon}_{11} x_2^l) \text{ (O5)} \\ Q_{66} 2 \bar{\epsilon}_{12}^l = \rho \frac{S_B}{b_B} \bar{a}_2^S \text{ (O6)} \end{cases} \quad (18)$$

epoxy or multi-directional laminates, this equation would be exploitable and the simplified equation would be biased.

Section Transverse to the Fibres

A section transverse to the fibres (right-hand side of Fig. 9) can also be considered. This will involve stiffness components Q_{11} , Q_{12} and Q_{66} . The following virtual fields are considered (same as those in Eq. 10, only in a different reference frame):

$$\begin{cases} u_1^{(1)*} = 1; u_2^{(1)*} = 0 \\ u_1^{(2)*} = 0; u_2^{(2)*} = 1 \\ u_1^{(3)*} = x_2; u_2^{(3)*} = -x_1 \end{cases} \quad (16)$$

The next sections are aimed at validating these generalized stress-strain relationships using simulated and experimental data.

Validation on Simulated Data

A finite element model was developed using ABAQUS Explicit. The reason for switching from LS-DYNA to ABAQUS was that some inconsistencies were found in the LS-DYNA results when attempting to validate the generalized stress-strain relationships. This is currently unresolved. In all other aspects, the model was similar to the isotropic one. The in-plane dimensions were $70 \times 44 \text{ mm}^2$, with a 1 mm thickness. The elements were CPS4R (4-node,

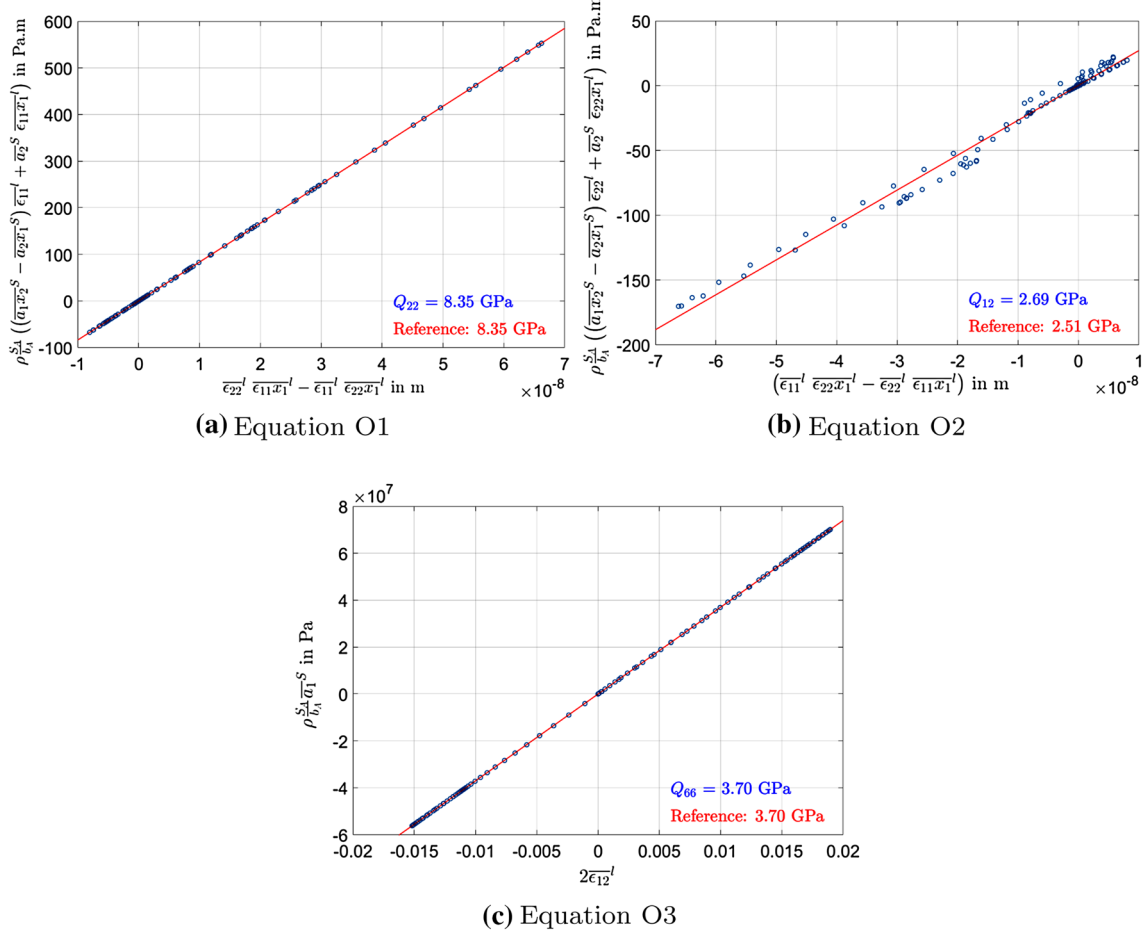


Fig. 10 Validation on FE generated orthotropic data, 45° off-axis test, central section parallel to the fibres, Eq. 14

reduced integration, plane stress). The mesh consisted of 280×176 elements². The time step was floating at $0.8 t_{crit}$ and beta damping of 1.10^{-8} s was employed. The data were output every $0.5 \mu\text{s}$ mimicking the experimental frame rate (see next section). A fibre angle of 45° was selected, with in-plane stiffness components close to the material in the experiment described in the next section: $Q_{11} = 124.7 \text{ GPa}$, $Q_{22} = 8.35 \text{ GPa}$, $Q_{12} = 2.51 \text{ GPa}$ and $Q_{66} = 3.70 \text{ GPa}$. The loading was applied through a triangular compressive pressure pulse rising to 300 MPa in $9 \mu\text{s}$ and decreasing back to zero in the same amount of time. The pressure was uniformly distributed over the specimen edge, contrary to the isotropic simulation. The off-axis configuration was found to be sufficient to ensure enough stress and strain heterogeneity so that none of the generalized stress-strain equations degenerated into zero equals zero.

Contrary to the isotropic example, acceleration averages have to be calculated over an irregularly shaped area, while strain averages need to be obtained along angled slices. It was therefore necessary to perform data interpolation. This will also be the case for the experimental data which are

obtained on a regular grid of points. The Matlab® ‘scattered-interpolant’ command was used (linear scattered interpolant) to calculate strain values over angled sections at 45°. The number of data points along each angled slice was kept the same as the number of points in a vertical slice, so as not to ‘overinterpolate’. The effect of interpolation parameters on the accuracy of the results is beyond the scope of the present paper but will have to be studied in the future. Only the slices of constant length were kept to ensure that enough data were averaged. Therefore, only a number of sections in the central part of the specimen were considered. They cover a length of 26 mm of the 70 mm of the specimen, for both sets of slices. To calculate the acceleration averages, a first test was performed to check whether the centroid of a given element was inside the considered area (S_A or S_B according to Fig. 9). The average was then calculated only from the elements inside the area. This resulted in a ‘staircase’ pattern which was deemed to be a reasonable approximation for the present validation. Split elements could be considered *prorata* in the future. The detailed interpolation procedure

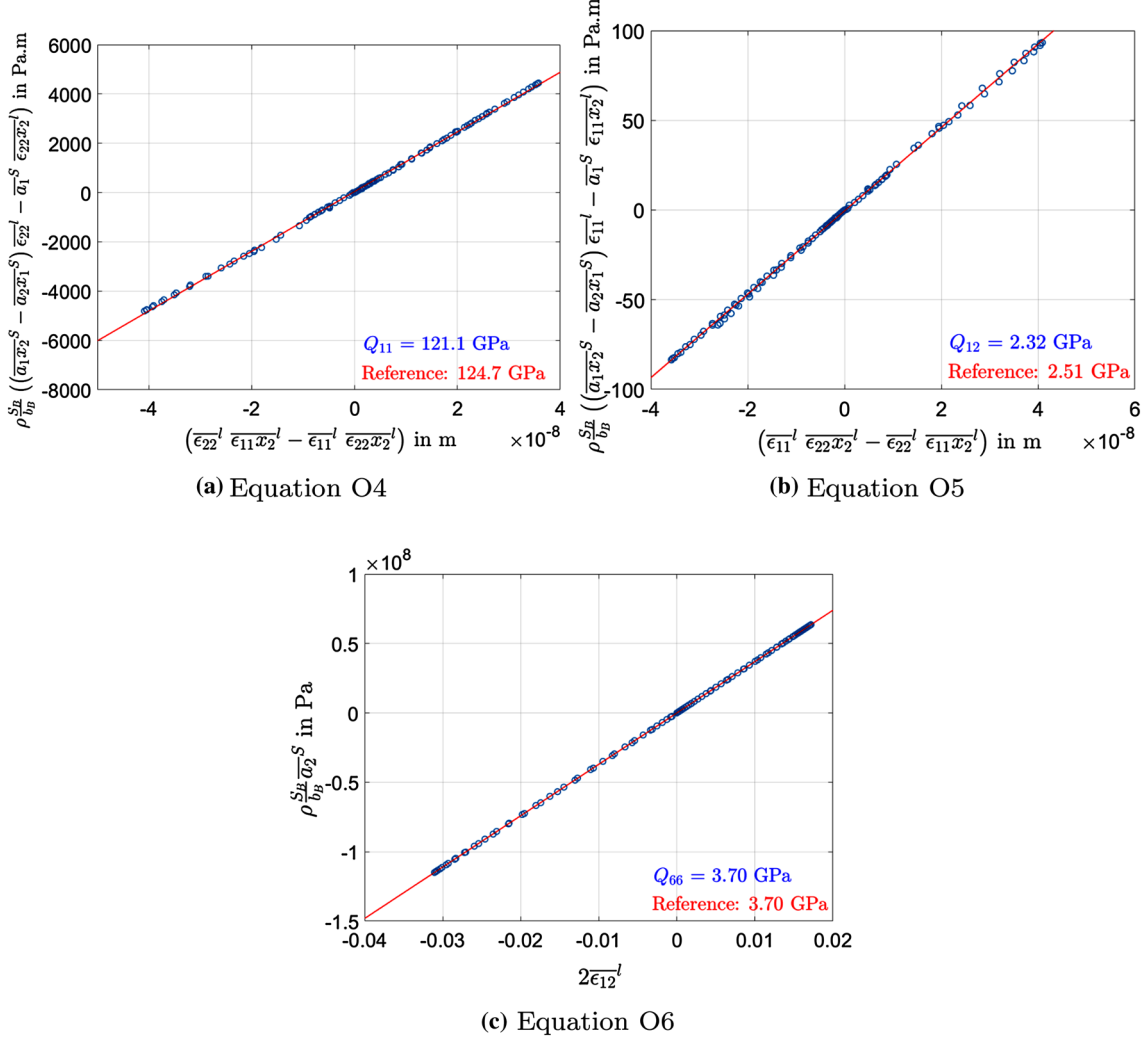


Fig. 11 Validation on FE generated orthotropic data, 45° off-axis test, central section transverse to the fibres, Eq. 18

can be found in the Matlab® routines provided in the data repository linked to this article.

The results for the central section parallel to the fibres can be found in Fig. 10. Both generalized stress-strain curves for Q_{22} and Q_{66} are perfectly linear and provide the reference stiffness exactly. Some scatter can be seen for Q_{12} however. The reason is that the strains in the fibres caused by Poisson's effect are very small as this relates to the minor Poisson's ratio which is an order of magnitude smaller than the major one for such an anisotropic material. This is why tensile tests at 0° and not 90° are employed to identify Poisson's ratio for unidirectional composites. So these data will be more prone to small numerical FE errors as well as interpolation biases. In practical experiments, this equation is unlikely to provide any useful information for such a material, though it may for less anisotropic materials like unidirectional glass/epoxy composites. The other interesting result is to investigate how

good the approximated relationship $OS1$ is compared to the full equation $O1$. The data have not been plotted here as they provide an equally perfect linear response, though the modulus only comes to 8.32 GPa instead of 8.35 GPa. This 0.3% error is negligible and equation $OS1$ can be confidently used here.

The sections transverse to the fibres are now considered. The results are plotted in Fig. 11, also for the central section. The results show again near perfect linearity, thus validating the relationships proposed here. One can see that Q_{12} , though exhibiting better linearity than for the parallel slice, still leads to a bias on the identified value of about 10%. The reason for this is that the strains in the fibres are already quite small in this configuration, and therefore, even if Poisson's effect is more significant, the related strains are even smaller. Again, the bias most probably arises from some interpolation error and/or small FE numerical errors. In practice, it is clear that this configuration is suboptimal to

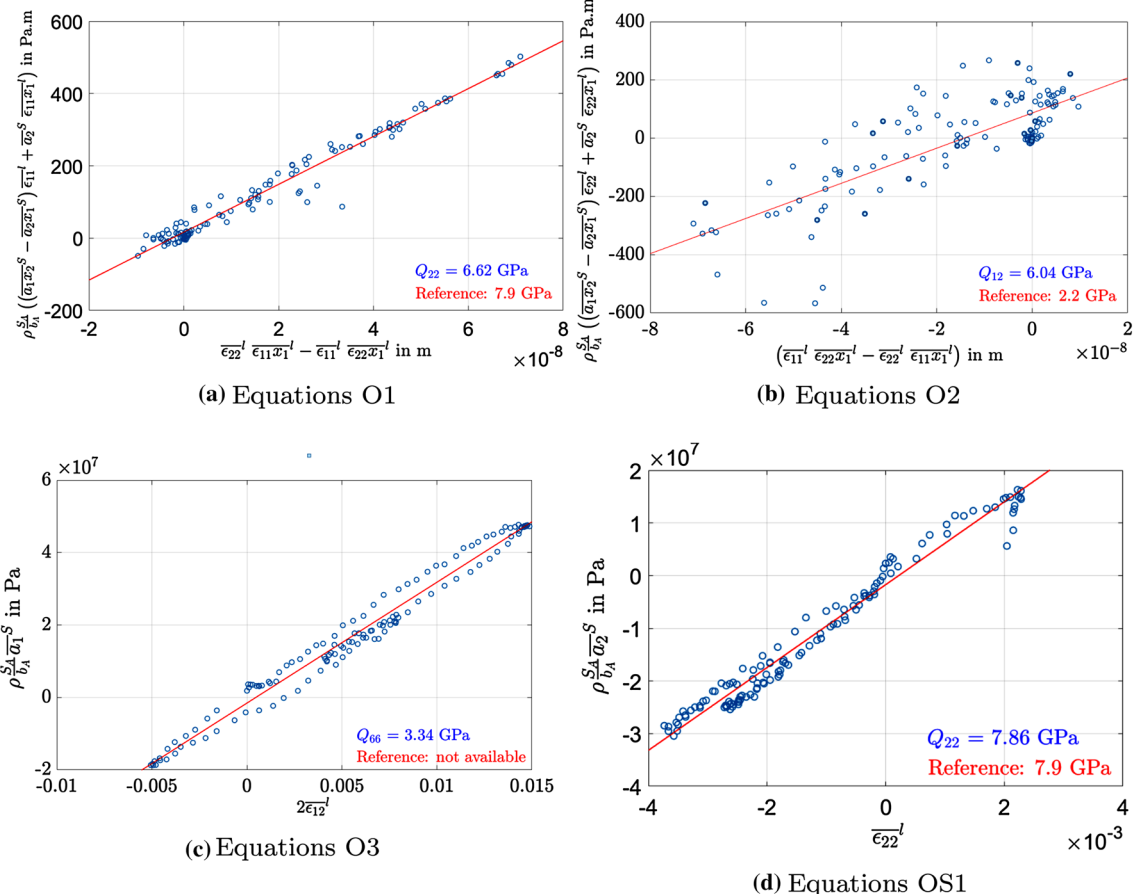


Fig. 12 Validation on experimental orthotropic data, section parallel to the fibres, 45° test, Eqs. 14 and 15

identify Q_{11} and therefore, Q_{12} . A shallower angle would have to be used. However, the present results are enough to validate the generalized stress-strain relationships.

Validation on Experimental Data

The final step is to validate the generalized stress-strain relationships on experimental data. A $70 \times 43 \text{ mm}^2$ carbon/epoxy unidirectional composite specimen was cut at 45° from a 3.72 mm $[0]_{12}$ panel autoclaved from GURIT SE70 prepreg. The material density was measured to $1530 \pm 25 \text{ kg.m}^{-3}$. One of the 43 mm specimen edges was bonded onto a cylindrical aluminium wave guide of diameter 45 mm and length 50 mm . The wave guide was then impacted using a cylindrical aluminium projectile of diameter 45 mm and length 25 mm . The nominal impact speed was 50 m.s^{-1} . The role of the wave guide is to improve the input of the stress wave into the specimen, and is also used to hold the sample in place before and during the test. A grid of 0.9 mm pitch was printed onto the specimen using a flat bed printer. This grid was imaged at 2 Mfps during the test with a Shimadzu HPV-X camera, and the grid images processed

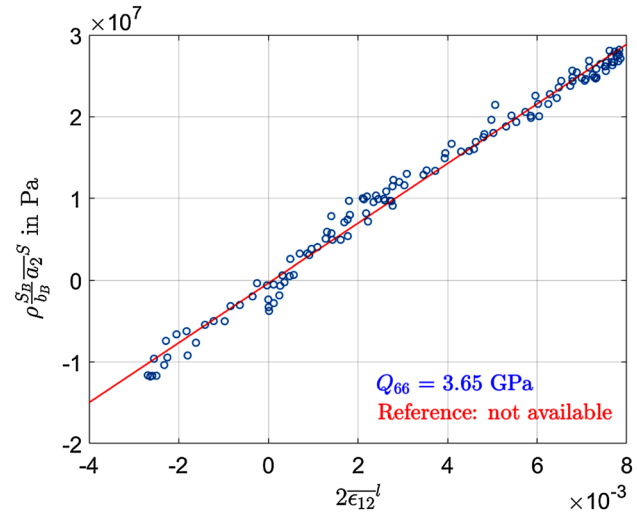


Fig. 13 Validation on experimental orthotropic data, section transverse to the fibres, 45° test, Eq. 18, O6

using spatial phase shifting [8]. All kinematic data are transformed from the specimen coordinate system to the material one using standard vector and tensor transformation.

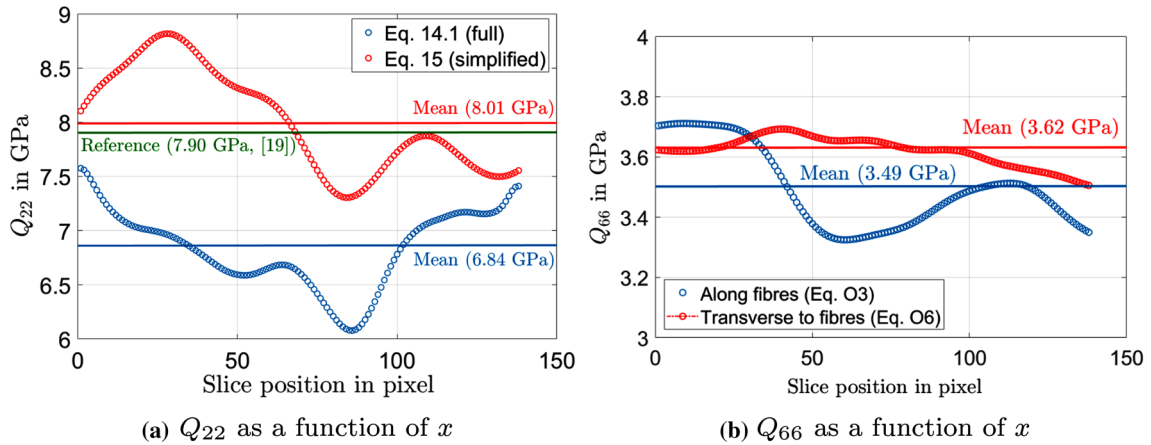


Fig. 14 Validation on experimental orthotropic data, 45° test, variation of identified stiffness along specimen length

More information about the setup, specimen positioning, illumination, triggering and image processing can be found in [19, 28]. During the first part of the test, an incoming compression wave is imparted to the specimen, which upon reflection off the free edge, turns into a tensile wave. This unloads the specimen and eventually generates enough local tension to crack the specimen along the fibres. It is beyond the present paper to analyse fracture, which here will be the result of a combination of transverse tension and shear. This will be the objective of a future study. It is noted here that the strength identification for the off-axis case will follow a similar analysis to that presented in [19] for a 90° test. The data from this test were processed using the generalized stress-strain relationships proposed in this study. First, slices parallel to the fibres have been investigated and the results have been plotted in Fig. 12 for the central slice.

The response for Q_{22} is nicely linear but provides a somewhat lower stiffness value than expected from the extensive 90° test campaign reported in [19] in which a value of 7.9 GPa was identified at similar strain rates (about 1000 s^{-1}). Interestingly, when the simplified relationship (OS1) of Eq. 15 is considered, the response provides the correct stiffness. This suggests that the small terms in Eq. 14 generate a bias, while the response remains linear. This is somewhat surprising and will have to be studied in more detail using synthetic image deformation as in [20]. The Q_{12} response, as expected, does not provide anything useful, justifying the fact that Poisson's effect along the fibre is indeed too small to be measured. This is also an *a posteriori* justification of the fact that the OS1 approximation is valid. Finally, the shear plot exhibits what could be seen as a slightly non-linear response with a hysteresis loop. However, looking at the shear response obtained from the central slice across the fibres, O6 in Eq. 18, plotted in Fig. 13, a perfectly linear relationship is found. It should be noted that the other sections showed similar trends. At this stage, the reason for

this remains unknown and will have to be investigated by undertaking more tests in the future. As also expected, no significant response could be obtained for Q_{11} and Q_{21} as this 45° configuration does not generate enough fibre strains to be able to measure them with sufficient accuracy. Tests on shallower angle specimens will be conducted in the future, even though the fibre stiffness is known to exhibit little strain rate dependence and is therefore a less critical parameter to study [29]. This is why this first feasibility test was conducted at 45° to concentrate on Q_{22} and Q_{66} .

In order to understand how stable the identified stiffnesses are as a function of the considered slices, the evolution of both Q_{22} and Q_{66} along x have been plotted in Fig. 14. The results are generally consistent, with some variations thought to be mainly caused by measurement noise. The data confirms that the simplified OS1 equation for Q_{22} provides a much more accurate identification, while the full equation (O1) leads to a bias of about 15%. Concerning Q_{66} , the values are much more stable for the slices across the fibres, the ones that exhibited a more linear response. This looks consistent, even though the exact cause is unknown at this stage. It should also be noted that the quasi-static shear modulus is not known for this material, so the identified values here cannot be checked against a quasi-static reference. Nevertheless, the present results show the practical relevance of the stress-strain relationships developed here, even if more research is required to better understand their sensitivity to noise.

Conclusion and Future Work

This paper has presented a set of new relationships to directly extract stiffness components for isotropic and orthotropic elasticity from Image-Based Inertial Impact (IBII) tests. The underpinning novelty of this test is to derive the stress information from the measured full-field acceleration so that

all required data are embedded in the recorded images. The purpose of this article was only to derive these generalized stress-strain relationships and to validate them on simulated data. The addition of actual experimental data provided an understanding of how useful they would be in practice. The main advantages of the present processing technique are:

- Compared to existing processing methods for the IBII test, these new relationships provide a step forward. They are more extensive than the simple ‘stress-gauge’ version presented initially in [9]. They do not need to assume Poisson’s ratio as was previously the case with the standard stress-gauge. The new equations allow the different stiffness components to be retrieved directly from various combinations of averages of the kinematic fields. For the first time, they have been successfully applied to an off-axis IBII test on a unidirectional composite.
- They are analytical and so, no complex inverse identification is required. They can be run as a quick diagnostic just after a test to evaluate the quality of the data.
- They provide spatially-resolved stiffness information without the need for parametrization. This is ideal to study the development of damage for instance.
- These relationships can help understand the consistency of the data, as illustrated in Fig. 8.

They exhibit clear limitations however, as reported below:

- They consider linear-elastic behaviour only, so would generally only apply to brittle or quasi-brittle materials. However, they can still be useful to study the transition between elasticity and say, plasticity or damage, as the earlier part of the response will generally be linear elastic. The stress equations like Eq. 2, 3 and 4 can also be used in the non-linear Virtual Fields Method [18, 22].
- They are limited to IBII-like configurations, in which only one specimen edge is loaded. This enables the use of rigid-body-like virtual fields without introducing another unknown stress distribution at the other end of the considered slice. They will also apply to the IBUS test configuration [23]. Some work is underway on this. They may also be extended to ‘anvil-like’ tests with loads at both ends, when considering the wave dominated regime. This will be investigated in the future.

Future work will concentrate on exploiting these relationships for off-axis tensile specimens, using both the IBII and IBUS tests. Synthetic image deformation [20] will be used to investigate how imaging error sources propagate in the generalized stress-strain quantities. There is also an opportunity to use the stress Eqs. 2, 3 and 4 in conjunction with free-edge boundary conditions to derive higher order polynomial stress approximations along the angled slices,

extending the methodology presented in Section ‘Virtual Fields for Strength Identification’ in [19]. This would allow for an improved approximation of the local stress state where the sample fails (in a similar manner to the linear stress-gauge presented in [19]). It is complementary to current research on the spatially-resolved reconstruction of stress from acceleration [30].

Finally, it is clear that these are still early days in the design and exploitation of image-based transient dynamic tests and that many opportunities are opening up with the availability of quality ultra-high speed cameras. This work is a step towards this long-term goal which will provide the next generation of high strain rate tests beyond the current split Hopkinson bar methodologies.

Data Provision

Data supporting this study are openly available from the University of Southampton repository at <https://doi.org/10.5258/SOTON/D0915>.

Acknowledgements The authors would like to thank Mr Jared Van Blitterswyk for his contribution to edge data reconstruction and for preparing the composite sample used for the off-axis tests.

Funding The authors acknowledge support from EPSRC through Grant EP/L026910/1 (Established Career Fellowship) as well as from the Air Force Research Laboratory, under agreement number FA9550-15-1-0293. The U.S. Government is authorized to reproduce and distribute reprints for Governmental purposes notwithstanding any copyright notation thereon. The views and conclusions contained herein are those of the authors and should not be interpreted as necessarily representing the official policies or endorsements, either expressed or implied, of the Air Force Research Laboratory or the U.S. Government. The authors would like to thank Dr David Garner (EOARD) for supporting this work.

Open Access This article is distributed under the terms of the Creative Commons Attribution 4.0 International License (<http://creativecommons.org/licenses/by/4.0/>), which permits unrestricted use, distribution, and reproduction in any medium, provided you give appropriate credit to the original author(s) and the source, provide a link to the Creative Commons license, and indicate if changes were made.

References

1. Kendall MJ, Siviour CR (2014) Experimentally simulating high-rate behaviour: rate and temperature effects in polycarbonate and PMMA. *Philos Trans Royal Soc A*. <https://doi.org/10.1098/rsta.2013.0202>
2. Field JE, Walley SM, Proud WG, Goldrein HT, Siviour CR (2004) Review of experimental techniques for high rate deformation and shock studies. *Int J Impact Eng* 30(7):725–775
3. Etoh TG, Mutoh H (2005) An image sensor of 1 Mfps with photon counting sensitivity. *Proc SPIE* 5580:301–307
4. Tochigi Y, Hanzawa K, Kato Y, Kuroda R, Mutoh H, Hirose R, Tominaga H, Takubo K, Kondo Y, Sugawa S (2013) A

global-shutter CMOS image sensor with readout speed of 1-tpixel/s burst and 780-mpixel/s continuous. *IEEE J Solid-State Circuits* 48(1):329–338

5. Specialized imaging Kirana camera. <http://specialised-imaging.com/products/video-cameras/kirana>. Accessed 3 May 2019
6. Shimadzu HPV-X camera. <https://www.ssi.shimadzu.com/products/high-speed-video-camera/hyper-vision-hpv-x2.html>. Accessed 3 May 2019
7. Sutton MA, Orteu JJ, Schreier HW (2009) Image correlation for shape, motion and deformation measurements: basic concepts, theory and applications. Springer, New-York
8. Grédiac M, Sur F, Blaysat B (2016) The grid method for in-plane displacement and strain measurement: a review and analysis. *Strain* 52(3):205–243
9. Pierron F, Zhu H, Siviour C (2014) Beyond Hopkinson's bar. *Philos Trans Royal Soc A* 372(2023):20130195
10. Aloui S, Othman R, Poitou A, Guégan P, El-Borgi S (2008) Non-parametric identification of the non-homogeneous stress in high strain-rate uni-axial experiments. *Mech Res Commun* 35(6):392–397
11. Moulart R, Pierron F, Hallett SR, Wisnom MR (2009) Full-field strain measurements at high rate on notched composites tested with a tensile Hopkinson bar. *Exp Mech* 3:1663–1668
12. Moulart R, Pierron F, Hallett SR, Wisnom MR (2011) Full-field strain measurement and identification of composites moduli at high strain rate with the virtual fields method. *Exp Mech* 51(4):509–536
13. Pierron F, Forquin P (2012) Ultra high speed full-field deformation measurements on concrete spalling specimens and stiffness identification with the Virtual Fields Method. *Strain* 28(5):388–405
14. Yoon S-H, Giannakopoulos I, Siviour CR (2015) Application of the virtual fields method to the uniaxial behavior of rubbers at medium strain rates. *Int J Solids Struct* 69–70:553–568
15. Yoon S-H, Winters M, Siviour CR (2016) High strain-rate tensile characterization of EPDM rubber using non-equilibrium loading and the Virtual Fields Method. *Exp Mech* 56(1):25–35
16. Yoon S-H, Siviour CR (2017) Application of the Virtual Fields Method to rubbers under medium strain rate deformation using both acceleration and traction force data. *J Dyn Behav Mater* 3(1):12–22
17. Yoon S-H, Siviour CR (2018) Application of the virtual fields method to a relaxation behaviour of rubbers. *J Mech Phys Solids* 116:416–431
18. Dreuilhe S, Davis F, Siviour CR, Pierron F (2017) Image-based inertial impact tests on an aluminum alloy. *Conf Proc Soc Exp Mech Ser* 3:219–223
19. Fletcher L, Van Blitterswyk J, Pierron F (2019) A novel image-based inertial impact (IBII) test for the transverse properties of composites at high strain rates. *J Dyn Behav Mater* 5(1):65–92
20. Fletcher L, Pierron F (2018) An image-based inertial impact (IBII) test for tungsten carbide cermets. *J Dyn Behav Mater* 4(4):481–504
21. Van Blitterswyk J, Fletcher L, Pierron F (2018) Image-based inertial impact test for composite interlaminar tensile properties. *J Dyn Behav Mater* 4:543–572
22. Dreuilhe S, Pierron F (2016) Extension of the non-linear virtual fields method to inertial heterogeneous high strain rate tests. *Conf Proc Soc Exp Mech Ser* 4:83–87
23. Seghir R, Pierron F (2018) A novel image-based ultrasonic test to map material mechanical properties at high strain-rates. *Exp Mech* 58(2):183–206
24. Koohbor B, Kidane A, Lu W-Y (2016) Effect of specimen size, compressibility and inertia on the response of rigid polymer foams subjected to high velocity direct impact loading. *Int J Impact Eng* 98:62–74
25. Forquin P, Lukic B (2018) On the processing of spalling experiments. Part I: Identification of the dynamic tensile strength of concrete. *J Dyn Behav Mater* 4(1):34–55
26. Piro JL, Grédiac M (2004) Producing and transferring low-spatial-frequency grids for measuring displacement fields with moiré and grid methods. *Exp Tech* 28(4):23–26
27. Zhu H, Pierron F (2016) Exploration of Saint-Venant's principle in inertial high strain rate testing of materials. *Exp Mech* 56(1):3–23
28. Fletcher L, Van-Blitterswyk J, Pierron F (2018) Combined shear/tension testing of fibre composites at high strain rates using an image-based inertial impact test. In: proceedings of EPJ Web of Conferences, vol. 183
29. Harding J, Welsh LM (1983) A tensile testing technique for fibre-reinforced composites at impact rates of strain. *J Mater Sci* 18(6):1810–1826
30. Seghir R, Pierron F, Fletcher L (2018) Image-based stress field reconstruction. In: proceedings of BSSM annual conference, 29–31 August 2018, Southampton, UK